

## Molecular Physics: An International Journal at the Interface Between Chemistry and Physics

Publication details, including instructions for authors and subscription information:

<http://www.tandfonline.com/loi/tmph20>

### Photoelectron angular distributions from rotationally state-selected $\text{NH}_3(\text{B}^1\text{E}'')$ : dependence on ion rotational state and polarization geometry

Paul Hockett<sup>a</sup>, Michael Staniforth<sup>a</sup> & Katharine L. Reid<sup>a</sup>

<sup>a</sup> School of Chemistry, University of Nottingham, Nottingham NG7 2RD, United Kingdom

Version of record first published: 15 Apr 2010

To cite this article: Paul Hockett, Michael Staniforth & Katharine L. Reid (2010): Photoelectron angular distributions from rotationally state-selected  $\text{NH}_3(\text{B}^1\text{E}'')$ : dependence on ion rotational state and polarization geometry, *Molecular Physics: An International Journal at the Interface Between Chemistry and Physics*, 108:7-9, 1045-1054

To link to this article: <http://dx.doi.org/10.1080/00268971003639266>

PLEASE SCROLL DOWN FOR ARTICLE

Full terms and conditions of use: <http://www.tandfonline.com/page/terms-and-conditions>

This article may be used for research, teaching, and private study purposes. Any substantial or systematic reproduction, redistribution, reselling, loan, sub-licensing, systematic supply, or distribution in any form to anyone is expressly forbidden.

The publisher does not give any warranty express or implied or make any representation that the contents will be complete or accurate or up to date. The accuracy of any instructions, formulae, and drug doses should be independently verified with primary sources. The publisher shall not be liable for any loss, actions, claims, proceedings, demand, or costs or damages whatsoever or howsoever caused arising directly or indirectly in connection with or arising out of the use of this material.

## INVITED ARTICLE

### Photoelectron angular distributions from rotationally state-selected $\text{NH}_3(\text{B}^1\text{E}'')$ : dependence on ion rotational state and polarization geometry

Paul Hockett†, Michael Staniforth and Katharine L. Reid\*

*School of Chemistry, University of Nottingham, Nottingham NG7 2RD, United Kingdom*

*(Received 24 November 2009; final version received 19 January 2010)*

By using high-resolution photoelectron velocity map imaging and a pump–probe ionization scheme we are able to demonstrate that photoelectron angular distributions from ammonia depend sensitively on the neutral rotational level that is ionized, and on the rotational level of the ion that is formed. We use this sensitivity to fully determine the photoionization dynamics giving rise to the observed photoelectron angular distributions and rotational branching ratios. In addition, we observe the dependence of the photoelectron angular distributions on initially prepared alignment, by varying the relative polarizations of pump and probe. This dependence can be used to corroborate the determined photoionization dynamics, and also provides a demonstration that tomographic reconstruction can be used to recreate three-dimensional photoelectron distributions in non-cylindrically symmetric situations.

**Keywords:** photoelectron spectroscopy; laser spectroscopy; intramolecular dynamics; orientation and alignment

#### 1. Introduction

The simplest example of a photofragmentation process involves the ejection of an electron from an atom or molecule. The dynamics are simple because the photoelectron carries away almost all of the released kinetic energy and has no internal degrees of freedom. However, because the photoelectron has such a long de Broglie wavelength quantum mechanical effects are the rule rather than the exception, showing up with particular splendour in photoelectron angular distributions (PADs) whose shapes result from the interference of scattered partial waves. In the case of molecular photoionization, PADs depend on the rotational state of the molecule prior to ionization, and also on the rotational state of the ion subsequently formed. Therefore, a rotationally resolved ‘state-to-state’ pump–probe photoionization experiment in which PADs are measured contains immense detail on the scattering dynamics which control the amplitudes and phases with which the partial waves are born. To date the achievement of rotational resolution in the methods of photoelectron spectroscopy required for the determination of PADs has been a serious experimental challenge, and until very recently [1] had been limited to diatomic molecules [2–5].

Velocity-map imaging (VMI) of photoelectrons, in which electric fields are used to direct photoelectron trajectories onto a position-sensitive detector, has gained enormous impetus since its first demonstration by Eppink and Parker [6]. This technique has 100% collection efficiency and provides ‘instant’ information on photoelectron angular distributions, however its drawback has been limitations on the achievable energy resolution. In VMI the resolution  $\Delta E$ , expressed in terms of photoelectron kinetic energy  $E$ , deteriorates rapidly as  $E$  increases. Because in many VMI experiments the pump and probe wavelengths are the same,  $E$  is constrained, limiting the achievable energy resolution. However, it has recently been shown that a judicious use of a second colour for the photoionization step can enable features as close as  $2\text{ cm}^{-1}$  to be distinguished [7]. To achieve this it is necessary to expand the photoelectron cloud to fill the detector by the choice of appropriate voltages, so that the number of pixels separating each photoelectron peak in the CCD image is maximized [8, 9]. As a consequence, any photoelectrons that are generated with higher energy than those of interest fall beyond the edges of the detector, and only a subset of the ‘full’ velocity map image is collected. The ability to distinguish features separated by  $2\text{ cm}^{-1}$  indicates the potential to resolve rotational structure in light polyatomic ions.

\*Corresponding author. Email: [katharine.reid@nottingham.ac.uk](mailto:katharine.reid@nottingham.ac.uk)

†Current address: Steacie Institute for Molecular Sciences, National Research Council of Canada, 100 Sussex Drive, Ottawa, Ontario K1A 0R6, Canada.

In the work described here we employ two-colour photoelectron VMI to the study of the photoionization dynamics of  $\text{NH}_3(\tilde{\text{B}}^1\text{E}'')$ . We expand on a previous publication in which we presented PADs resulting from the ionization from two rotational levels in the  $v_2=4$  state and associated with resolved rotational levels of the ground state of the cation [1]. Here, we present PADs for a series of selected and detected rotational states, and also illustrate the additional information that can be obtained by changing the alignment of the prepared  $\tilde{\text{B}}^1\text{E}''$  state rotational level. In a future publication we will consider the effects of changing the  $\tilde{\text{B}}^1\text{E}''$  state vibrational level, and the photoelectron kinetic energy, on the dynamics observed [10].

## 2. Preliminaries

The  $\tilde{\text{B}}^1\text{E}''$  electronic state of ammonia is an  $n=3$  Rydberg state in which the atoms adopt a planar geometry, and lies  $59,225\text{ cm}^{-1}$  [11] above the  $\tilde{\text{X}}^1\text{A}_1'$  pyramidal ground state. This state can be accessed by the absorption of two photons in the near-UV. The change in geometry on excitation generates favourable Franck–Condon factors for the formation of the  $\tilde{\text{B}}^1\text{E}''$  state with relatively high quanta in  $v_2$ , the ‘umbrella’ vibrational mode; thus  $v_2=4$  can be prepared with significant intensity. Strong parity, symmetry and angular momentum selection rules control the rotational levels that can be prepared following excitation to the  $\tilde{\text{B}}^1\text{E}''$  state ( $v_2=4$ ) [11]. In this work we study six rovibronic transitions labelled by  $N_K$  values of the initial ( $\tilde{\text{X}}^1\text{A}_1'$ ) and final ( $\tilde{\text{B}}^1\text{E}''$ ,  $v_2=4$ ) states:  $1_0 \rightarrow 1_1$ ,  $3_1$  and  $1_1 \rightarrow 1_0$ ,  $2_2$ ,  $3_0$ ,  $3_2$ .

The  $\tilde{\text{B}}^1\text{E}''$  state electronic character is known to be predominantly  $p\pi$  with a small contribution of  $d\delta$  character, but the exact ratio of the two is not known [12, 13]. The Rydberg series of which the  $\tilde{\text{B}}^1\text{E}''$  state is a member converges on the  $\tilde{\text{X}}^2\text{A}_2''$  ground state of the cation and therefore there is a strong propensity for the vibrational state to be unchanged on photoionization to the  $\tilde{\text{X}}^2\text{A}_2''$  state. The adiabatic ionization potential of  $\text{NH}_3$  has been determined to be  $82,158.75 \pm 0.016\text{ cm}^{-1}$  [14], with the  $v_2^+=4$  level lying at  $85,966.4\text{ cm}^{-1}$  [15]. The approximate total photon energy used in our experiments is  $\sim 86,226\text{ cm}^{-1}$  (depending on the  $\tilde{\text{B}}^1\text{E}''$  state rotational level selected), giving a maximum possible kinetic energy of  $\sim 300\text{ cm}^{-1}$  for those photoelectrons whose creation leaves the ion in  $v_2^+=4$ . On one-photon photoionization from the  $\tilde{\text{B}}^1\text{E}''$  state a number of selection rules constrain the photoelectron partial waves that can be formed in conjunction with a given ion rotational state [16];

Table 1. Allowed partial waves for ionization from the  $\tilde{\text{B}}^1\text{E}''$  state level ( $v_2=4$ ,  $N_i$ ,  $K_i$ ) with formation of the  $\tilde{\text{X}}^2\text{A}_2''$  cation ground state in ( $v_2^+=4$ ,  $N^+$ ,  $K^+$ ).

$K_i$	$K^+$	$l$	$K_i$	$K^+$	$l$
0, 2	1	s, d, g, ...	1	0	s, d, g, ...
	2	p, f, h, ...		3	p, f, h, ...
	4	s, d, g, ...		6	s, d, g, ...
	5	p, f, h, ...			

these are summarized in Table 1. In addition, the atomic selection rule  $\Delta l = \pm 1$  is expected to give a propensity for the formation of partial waves with orbital angular momenta  $l=0$  and  $2$  ( $s$  and  $d$ ) which would be associated with the  $p\pi$  character of the  $\tilde{\text{B}}^1\text{E}''$  state.

In the  $(2+1')$  scheme used in this work symmetry requires that the measured photoelectron intensity as a function of angle must obey the equation [17]

$$I(\theta, j) = \beta_{00} \left\{ 1 + \sum_{M=-2}^2 \beta_{2M} Y_{2M}(\theta, \varphi) + \sum_{M=-4}^4 \beta_{4M} Y_{4M}(\theta, \varphi) + \sum_{M=-4}^4 \beta_{6M} Y_{6M}(\theta, \varphi) \right\}, \quad (1)$$

where  $\beta_{LM}$  are coefficients describing the angular intensity, and  $Y_{LM}(\theta, \phi)$  are spherical harmonic functions. A given  $\beta_{LM}$  coefficient can only have contributions from interfering pairs of photoelectron partial waves whose orbital angular momenta  $l$  and  $l'$  obey the condition  $|l-l'| \leq L \leq (l+l')$ . In the case where the linear polarization vectors of the exciting and ionizing light are parallel,  $M$  must be zero and there is no  $\phi$  dependence:

$$I(\theta, \varphi) = \beta_{00} \{ 1 + \beta_{20} Y_{20}(\theta, 0) + \beta_{40} Y_{40}(\theta, 0) + \beta_{60} Y_{60}(\theta, 0) \}. \quad (2)$$

If the linear polarization vectors of the (two-photon) pump and (one-photon) probe are perpendicular to each other, then the rotation of the distribution of rotational angular momentum vectors created by the pump laser into the frame of the probe laser allows  $M$  to take the values 0, 2 and 4 (see the appendix), giving

$$I(\theta, \varphi) = \beta_{00} \{ 1 + \beta_{20} Y_{20}(\theta, \varphi) + 2\beta_{22} Y_{22}(\theta, 0) \cos 2\varphi + \beta_{40} Y_{40}(\theta, \varphi) + 2\beta_{42} Y_{42}(\theta, 0) \cos 2\varphi + 2\beta_{44} Y_{44}(\theta, 0) \cos 4\varphi + \beta_{60} Y_{60}(\theta, \varphi) + 2\beta_{62} Y_{62}(\theta, 0) \cos 2\varphi + 2\beta_{64} Y_{64}(\theta, 0) \cos 4\varphi \}. \quad (3)$$

### 3. Experimental

We use the technique of photoelectron velocity map imaging (VMI) and focus on the slow electrons that can be generated by appropriate choice of ionization wavelength. Our VMI spectrometer follows the standard Eppink and Parker design [6], and has been described in detail elsewhere [18]. A 10% mixture of ammonia in argon was introduced into the spectrometer via a pulsed nozzle with a backing pressure of 2 bar, resulting in a molecular beam with a rotational temperature of approximately 15 K. Two laser beams (pump and probe) co-propagated perpendicular to the molecular beam and were loosely focused in the interaction region. Wavelengths in the range 317–318 nm were obtained from the frequency doubled output of a Continuum ND6000 dye laser (DCM in methanol) pumped by a Continuum Surelite III Nd:YAG laser. These wavelengths were used to prepare ammonia in rotationally selected levels of its  $B^1E''$ ,  $v_2=4$  state following the absorption of two pump photons. Wavelengths in the range 430–435 nm were obtained from the fundamental output of a Sirah Cobra dye laser (Exalite 428 in dioxane) pumped by the frequency tripled output of a Continuum Surelite I Nd:YAG laser. Ionization could then occur following the absorption of three pump photons ( $2+1$ ), or the absorption of two pump photons and one probe photon ( $2+1'$ ). For the final results presented here the probe wavelength was set to 431.52 nm, chosen (a) to produce photoelectrons that were free from the effects of continuum resonances [10], and (b) to optimize resolution so that ion rotational states could be distinguished.

The resulting photoelectrons were focussed by an electrostatic lens onto a position sensitive detector comprising two microchannel plates and a phosphor screen. In order to achieve rotational resolution the electrostatic lens voltages were set to 160 V (repeller,  $V_r$ ) and 108 V (extractor,  $V_e$ ). These were chosen to expand the photoelectron clouds resulting from the ( $2+1'$ ) ionization process so that they filled the detector, at the expense of those photoelectrons resulting from ( $2+1$ ) ionization which fell beyond the edges of the detector [8]. The phosphor emission was imaged using a CCD camera, resulting in photoelectron images. The laser beam propagation direction and the linear polarization vectors in the parallel polarization experiments were coincident with the plane of the detector; the molecular beam travelled perpendicular to the plane of the detector. In the crossed polarization experiments the linear polarization vectors of the pump and probe laser beams were set to be perpendicular, and photoelectron images were

measured for a series of 10 angles,  $\theta_D$ , between the probe laser polarization and the plane of the detector.

The photoelectron images contain information on the photoelectron spectrum, and on the PADs. For the parallel polarization geometry the photoelectron distribution has cylindrical symmetry which enables the images to be processed using the pBasex inversion routine [19]. The perpendicular polarization geometry is not cylindrically symmetry (see Equation (3)) meaning that this inversion method can no longer be used. In this case the three-dimensional photoelectron distribution was tomographically reconstructed from the set of photoelectron images measured at different  $\theta_D$  values in a manner analogous to that used by Baumert and coworkers [20]. A one pixel width column is taken at the same point in each of the 10 images to form a matrix which is input into the Matlab function 'iradon'. This reproduces a two-dimensional slice of the original three-dimensional distribution in the plane perpendicular to the detector. Once this has been achieved for every column in the image set, the full three-dimensional distribution can be reconstructed from the set of two-dimensional slices.

## 4. Results

### 4.1. Parallel polarization vectors

In all experiments photoelectrons are liberated following both one-colour ( $2+1$ ) and two-colour ( $2+1'$ ) ionization. In Figure 1(a) we show the image that is collected when all the photoelectrons generated for  $\lambda_{\text{pump}} = 317.20$  nm and  $\lambda_{\text{probe}} = 434.22$  nm are allowed to impinge on the detector (this is achieved by setting  $V_r = 2700$  V and  $V_e = 1874$  V). In Figure 1(b) the image that results from changing the voltages to  $V_r = 160$  V and  $V_e = 110$  V, chosen to expand the two-colour image to fill the detector, is shown. It can be seen that the reduction of the applied voltages allows the inner ring in Figure 1(a) to resolve into three rings in Figure 1(b). These three rings correspond to rotational levels of the ammonia cation ground state ( $v_2^+ = 4$ ).

In Figure 2, in which the optimized probe wavelength of 431.52 nm is chosen together with the reduced voltages used in Figure 1(b), the photoelectron images that result from the preparation of the six  $B^1E''$  state rotational levels are shown. In all cases clearly resolved rings can be seen that correspond to cation rotational levels. Each image shown in Figure 2 was inverted using the pBasex routine [19] to generate photoelectron spectra and  $\beta_{LM}$  coefficients, together with error bars, that describe the PAD corresponding to each ion rotational state. These  $\beta_{LM}$  coefficients can be used to generate polar plots of 'experimental' photoelectron



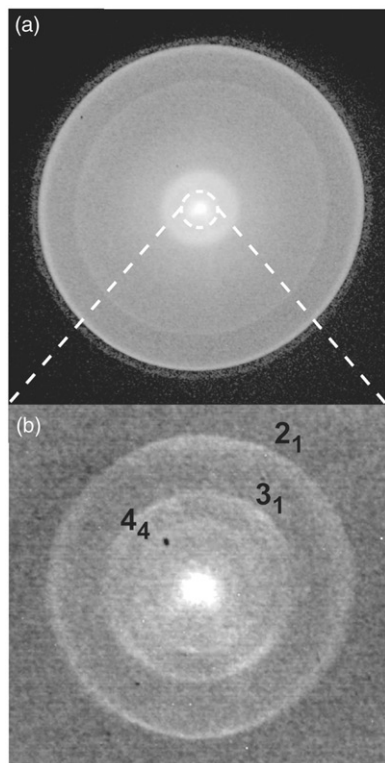


Figure 1. Illustration of how reducing the voltages on the VMI electrostatic plates improves resolution. (a) Photoelectron image showing outer rings corresponding to one-colour photoionization and a central ring corresponding to two-colour photoionization with  $V_r = 2700$  V and  $V_e = 1874$  V. (b) Expansion of the centre of the ring in (a) by lowering the voltages to  $V_r = 160$  V and  $V_e = 110$  V disperses the photoelectron according to the labelled ion rotational states.

intensity for each ion rotational state. The resulting extracted photoelectron spectra and angular distributions are shown in Figures 3 and 4 (solid lines). The error bars shown on the angular distributions can be seen to be small as a consequence of good statistics.

#### 4.2. Perpendicular polarization vectors

In the crossed polarization experiment only the  $1_1 \rightarrow 3_2$  rovibronic transition was studied. Photoelectron images were collected for 10 detection angles ( $\theta_D$ ) and the three-dimensional distributions tomographically reconstructed as described above. An example of a raw tomographically reconstructed PAD is shown in Figure 5(a). It can be seen that the noise levels in the reconstructed data are quite significant, causing it to appear jagged. Noise is also amplified in the  $z=0$  plane, which can give rise to artefacts in the reconstructed distributions (analogous to the amplification

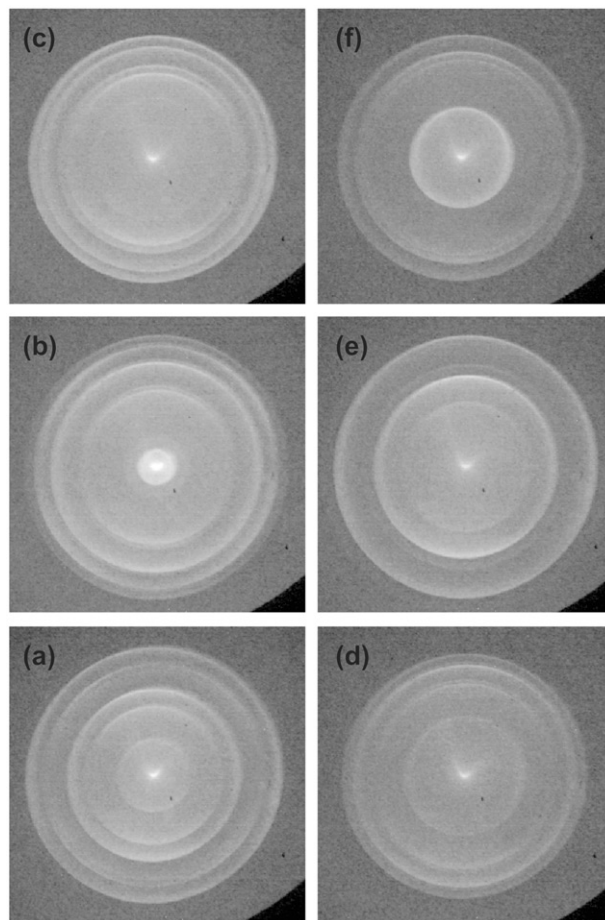


Figure 2. Rotationally resolved photoelectron images following the ionization of six B state rotational levels prepared by the  $\tilde{X}^1A'_1 \rightarrow \tilde{B}^1E''$  ( $v_2=4$ ) transitions: (a)  $1_1 \rightarrow 3_2$ , (b)  $1_1 \rightarrow 2_0$ , (c)  $1_1 \rightarrow 2_2$ , (d)  $1_1 \rightarrow 1_0$ , (e)  $1_0 \rightarrow 3_1$  and (f)  $1_0 \rightarrow 1_1$ .

of noise along the centre-line of Abel inverted images [19, 21]). The reconstructed three-dimensional distributions must obey Equation (3) by symmetry, and are fitted to this equation to generate 'experimental'  $\beta_{LM}$  coefficients.

The result of doing this is shown in Figure 5(b) where it can be seen that the fitting process removes the effects of random noise in the data. Fits corresponding to the three most intense and well-resolved ion rotational states formed following ionization of the  $3_2$  level in the  $\tilde{B}^1E''$  state are shown in Figure 6(a).

## 5. Discussion

The rotationally resolved photoelectron spectra (Figure 3) can be compared with spectra in the literature that have been obtained by other

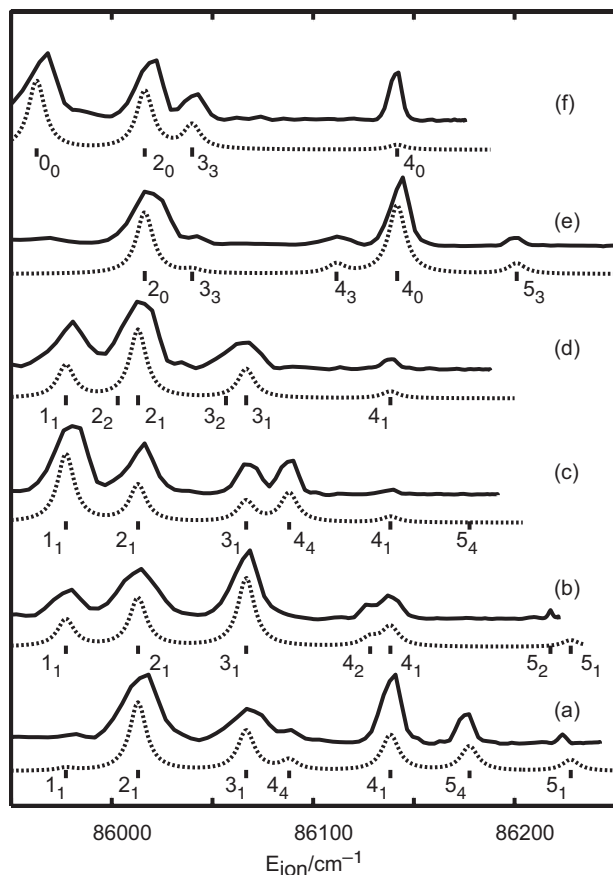


Figure 3. Solid line: photoelectron spectra extracted from the images shown in Figure 3, with labelled ion rotational states. Dashed line: predicted photoelectron spectra using the rotational branching ratios predicted from the parameters shown in Table 2, line positions from Ref. [14], and line broadening based on experimental resolution.

methods [12, 14]; this will be done in a subsequent publication in which more data is presented at different probe wavelengths [10]. Here, we concentrate on the photoelectron angular distributions which have not been measured before and which are most sensitive to details of the ionization dynamics. It is apparent from Figure 4 that the PADs are richly structured and highly sensitive to rotational level, both in the  $\tilde{B}^1E''$  state and in the ion. The sensitivity to  $\tilde{B}^1E''$  state rotational level had been observed previously [22], and is a consequence of the fact that (a) a different subset of ion rotational levels is formed following the ionization of each  $\tilde{B}^1E''$  state rotational level (see Figure 4) because of severe symmetry restrictions [16], and (b) a different alignment of rotational angular momentum vectors in the  $\tilde{B}^1E''$  state is prepared for different rovibronic transitions. An illustration of this sensitivity can be seen in Figure 7 in which the PADs corresponding to unresolved ion rotational states are presented; it can be

seen that the PADs change with initial  $N_K$  level. This effect is in contrast to what is seen in the ionization of diatomic molecules in which PADs show almost no change with *initial* (neutral) rotational level, but may show striking changes with *final* (ion) rotational level [4, 23].

In the case of ammonia the dependence of PADs on initial rotational level allows some dynamical information to be inferred [22], but the resolution of final rotational level unveils a whole new sensitivity that can be exploited. The strong dependence on both initial and final rotational level means that the PADs shown in Figure 4 contain a wealth of data, namely 28 independent values of each of the  $\beta_{00}$ ,  $\beta_{20}$ ,  $\beta_{40}$  and  $\beta_{60}$  coefficients (Equation (2)), where the  $\beta_{00}$  values provide the relative intensities of each ion rotational level. Such a wealth of data makes it tractable to fit the determined  $\beta_{LM}$  parameters *in the parallel geometry alone* to a model which contains variable parameters corresponding to the radial dipole matrix elements  $r_{l\lambda}$  and phases  $\eta_{l\lambda}$  that connect the  $\tilde{B}^1E''$  state ( $v_2=4$ ) to each  $l\lambda$  photoelectron partial wave, where  $\lambda$  denotes the projection of  $l$  on the molecular symmetry axis, and it is assumed that the rotational dependence of these radial dipole matrix elements can be expressed by purely geometrical (angular momentum coupling) terms. This approach has been used in earlier work [4, 24]. The expression used to fit the  $\beta_{LM}$  coefficients to  $r_{l\lambda}$  and  $\eta_{l\lambda}$  parameters is given in Equation (4) in the appendix, and is based on the formalism of Dixit and McKoy [25]. In this work we only fit the normalized  $\beta_{LM}$  coefficients with  $L > 0$ , and use the parameters resulting from the fit to predict the  $\beta_{00}$  values, and hence rotational branching ratios, for comparison with the photoelectron spectra shown in Figure 3. This provides a test of the fit.

The model that we use (see appendix) does not make any assumptions about the Rydberg character of the  $\tilde{B}^1E''$  state, but allows any photoelectron partial wave to be formed that is consistent with symmetry and angular momentum selection rules. This enables us to fit PADs corresponding to ion rotational levels whose formation is inconsistent with the 'atomic-like' ionization selection rules that are often applied in the case of Rydberg states. These ion rotational states result from the exchange of angular momentum following rescattering of the emitted photoelectron off the ion core. The model does however make some assumptions about the photoionization dynamics. We fit the whole data set shown in Figure 4 simultaneously to obtain a single set of parameters. This can only be done if there is no significant energy dependence to the photoionization dynamics over the small range studied. In addition, it is assumed that the photoelectron is

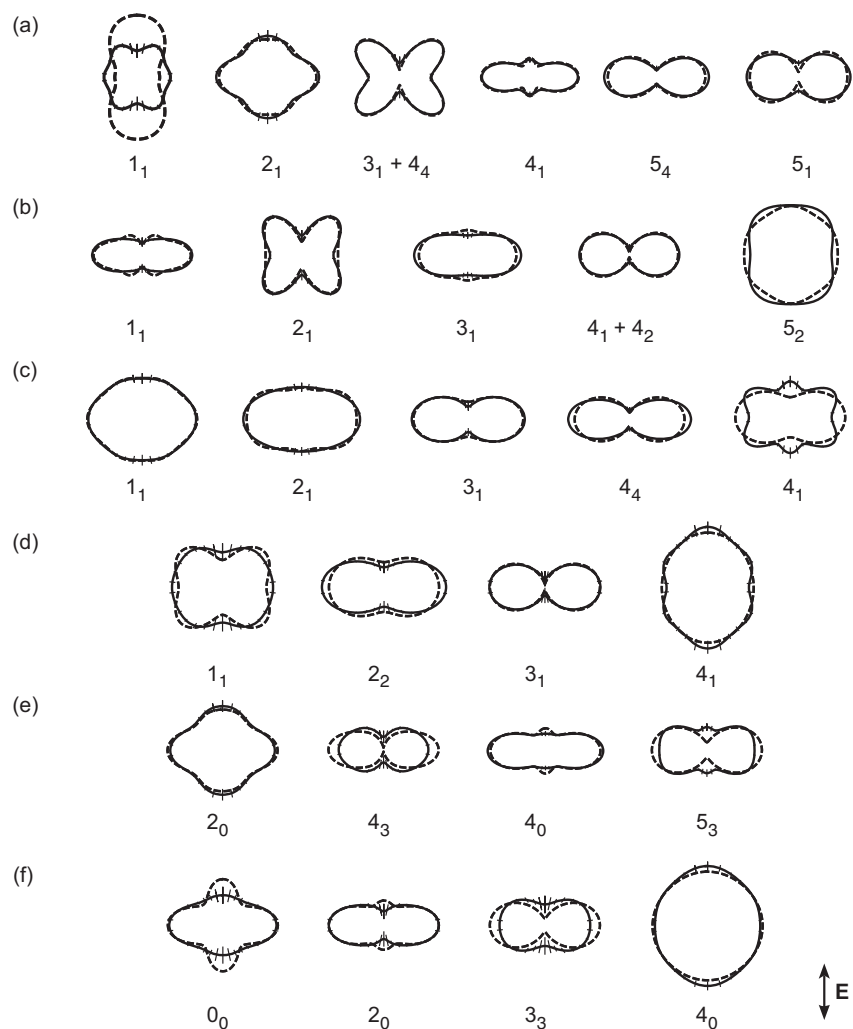


Figure 4. Normalized polar plots of photoelectron intensity relative to the linear polarization vector of the probe laser. Solid line: angular distributions plotted from the  $\beta_{LM}$  coefficients determined by inversion of the images shown in Figure 2 using the pBasex inversion routine. Dashed line: angular distributions predicted using the parameters shown in Table 2. (a) to (f) correspond to the  $\tilde{X}^1A_1' \rightarrow \tilde{B}^1E''$  ( $v_2=4$ ) transitions indicated in Figure 2. Ion rotational levels are labelled.

emitted on a timescale that is very short compared with a vibrational period. Because the ionization event can occur at any point during the vibrational motion, this means that the radial dipole matrix elements can be averaged over the vibrational wavefunction. Allowing for these constraints the parameters  $r_{l\lambda}$  and  $\eta_{l\lambda}$  are allowed to vary freely.

The final values of the parameters that result from the fit are shown in Table 2, and the resulting fitted PADs and predicted photoelectron spectra are shown in Figures 3 and 4 by dashed lines. The predicted photoelectron spectra are generated from the  $\beta_{00}$  values that are predicted using the parameters from the fit, with lines placed at the known transition wavenumbers [14], and broadened to simulate the widths observed in the experiment. It can be seen that

the fit reproduces well all of the 28 PADs shown in Figure 4 with the exception of two PADs corresponding to weak features in Figure 3 ( $1_1$  in Figure 4(a) and  $4_1$  in Figure 4(c)). Interestingly, these two features result from photoelectron rescattering as discussed above and would not be present if atomic-like selection rules were obeyed. In addition, the predicted branching ratios show good agreement with the photoelectron spectra shown in Figure 3 with the sole exception of the  $4_0$  ion peak seen in Figure 3(f), again a feature resulting from rescattering. This observation will be discussed in a subsequent publication [10]. The fit (Table 2) shows a significant contribution of  $l=4$  (g waves, 10.5%) to the photoelectron wavefunction which had not been anticipated in previous work [13, 22]. Although there are no ion rotational states formed that require  $l=4$ ,

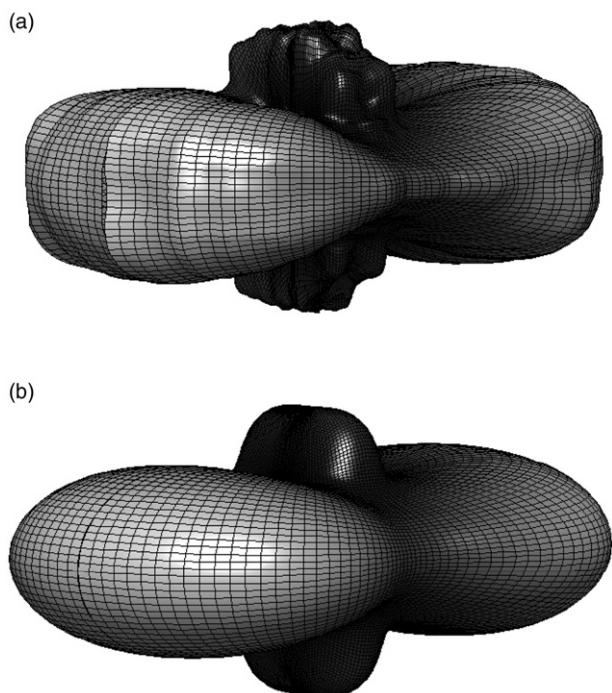


Figure 5. Example of (a) a tomographically reconstructed photoelectron distribution and (b) the smoothed version resulting from its fit to Equation (3). The example shown is the PAD corresponding to the  $3_1$  ion rotational level formed following photoionization of the  $3_2$  level in the  $\tilde{B}^1E''$  state ( $v_2=4$ ).

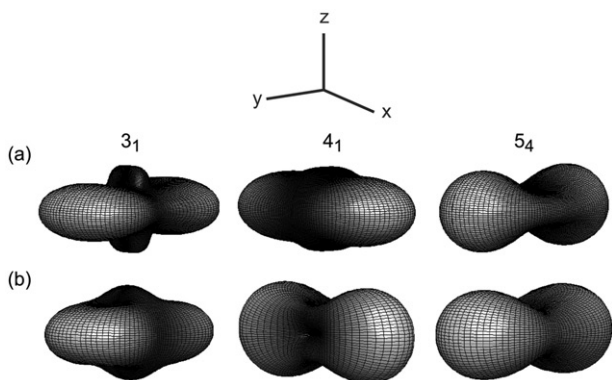


Figure 6. Comparison of (a) tomographically reconstructed and smoothed three-dimensional PADs with (b) the predictions resulting from the insertion of the parameter set shown in Table 2 into Equation (4). All distributions shown are for the  $1_1 \rightarrow 3_2$   $\tilde{X}^1A_1'' \rightarrow \tilde{B}^1E''$  ( $v_2=4$ ) transition, with labelled ion rotational states. The linear polarization vector of the probe laser beam is along the  $z$  axis.

and therefore the presence of  $g$  waves could not be inferred from a ZEKE or MATI spectrum [12, 14], their contributions are unambiguously shown by the anisotropies of some of the PADs. In particular, in order to make ion states with  $K=1$  or 5, selection rules

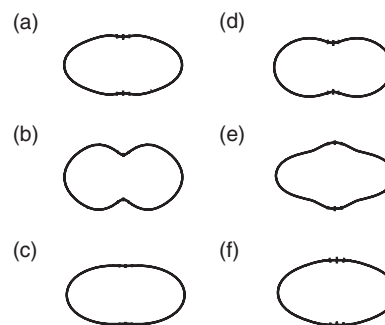


Figure 7. Polar plots of photoelectron intensity for the six  $\tilde{X}^1A_1'' \rightarrow \tilde{B}^1E''$  ( $v_2=4$ ) transitions indicated in Figure 2 with unresolved ion rotational states. These have been generated from a weighted sum of the rotationally resolved PADs that have been measured.

Table 2. Fitted magnitudes ( $r_{l\lambda}$ ) and relative phases ( $\eta_{l\lambda}$ ) of the radial dipole matrix elements for ionization with associated uncertainties. The  $\eta_{l\lambda}$  values include the Coulomb phase shifts,  $\sigma_l$ . The phases for odd  $l$  are relative to the  $p \pi$  phase; the phases for even  $l$  are relative to the  $s \sigma$  phase. The odd/even phase relationship cannot be determined unless parity is broken.

$l$	$\lambda$	$r_{l\lambda}$	$\eta_{l\lambda}$ (deg)	$r_{l\lambda}^2$ (%)	$F_l$ (%)
s	$\sigma$	0.357 (12)	$\equiv 0$	12.7 (17)	12.7 (17)
p	$\sigma$				13.0 (11)
	$\pi$	0.361 (8)	$\equiv 0$	13.0 (11)	
d	$\sigma$	0.137 (4)	31 (9)	1.9 (5)	53.0 (7)
	$\pi$	0.387 (2)	16 (3)	15.0 (3)	
	$\delta$	0.601 (3)	149 (2)	36.1 (4)	
f	$\sigma$				10.7 (2)
	$\pi$	0.084 (1)	162 (3)	0.7 (1)	
	$\delta$	0.143 (1)	153 (1)	2.1 (1)	
	$\phi$	0.282 (1)	153 (1)	8.0 (1)	
g	$\sigma$	0.171 (7)	92 (9)	2.9 (10)	10.5 (17)
	$\pi$	0.276 (8)	64 (23)	7.6 (12)	
	$\delta$	0.000 (5)		0.0	
	$\phi$				
	$\gamma$				

require that  $l$  must be even [16]. If a PAD has an anisotropy that requires a non-zero value of  $\beta_{60}$  then there must be a contribution from  $l \geq 3$ . Several strong ion peaks assigned to  $K=1$  and associated with PADs having  $|\beta_{60}| \gg 0$  are observed, thus requiring the presence of partial waves with *even* valued  $l \geq 4$ . The inclusion of  $l=6$  led to predicted rotational branching ratios that could not be reconciled with the experimental observations, whereas the inclusion of  $l=4$  was essential to reproduce the PADs. This example illustrates the necessity of obtaining angular information in order to make a full determination of ionization dynamics.



The parameters listed in Table 2 constitute a full characterization of the ionization event. It can be seen that although the photoelectron wavefunction is composed of  $\sim 66\%$  s and d waves, commensurate with the  $p\pi$  Rydberg character of the  $\tilde{B}^1E''$  state, there is a significant contribution from p, f and g waves. The former two can be explained as resulting from atomic-like ionization of the  $d\delta$  component of the  $\tilde{B}^1E''$  state, but the g wave can only result from a rescattering process in which the initially created photoelectron changes its angular momentum. It seems most likely that this is caused by the interaction of a d wave with a quadrupolar potential, although it is possible that the d wave may have a second-order interaction with the dipolar potential that will exist in bent geometries. The fit is extremely sensitive to the values of the phases,  $\eta_{l\lambda}$ , which dictate the positions of the nodes in the PADs caused by destructive interference between partial waves. These phases provide important information for Multichannel Quantum Defect Theory calculations [13], because they can be related to quantum defects for the relevant  $l\lambda$  Rydberg series as  $n \rightarrow \infty$  [26] which have not previously been determined for ammonia.

For most molecular photoionization processes it is expected that data taken in various polarization geometries will be necessary in order to make a full determination of photoionization dynamics [4, 27]. Therefore, the ability to deal with non-cylindrically symmetric PADs is a vital tool, and robust means need to be established. In the case of ammonia, because so much data has been obtained by resolving rotational levels in the  $\tilde{B}^1E''$  state and in the ion, the data taken in the crossed polarization geometry has not been required for the determination of the parameters shown in Table 2. This allows us to use these dynamical parameters, together with expression (4) given in the appendix, to calculate the PADs that would be expected to result in any polarization geometry. Therefore, the three-dimensional PADs that result from the fit to the tomographically reconstructed distribution when the pump and probe polarization vectors are perpendicular to each other can be compared with predicted distributions; such a comparison is shown in Figure 6. The fitted and calculated 3D distributions show reasonably good agreement which serves to corroborate the fitted parameter set, and demonstrates the predictive power of calculations based on these parameters. The converse is also true; the tomographic reconstruction technique is seen to produce results which are broadly as expected from the calculations. Thus, the data also provides a good test of the tomographic reconstruction technique. This technique has previously been demonstrated by Baumert and coworkers for the example of a

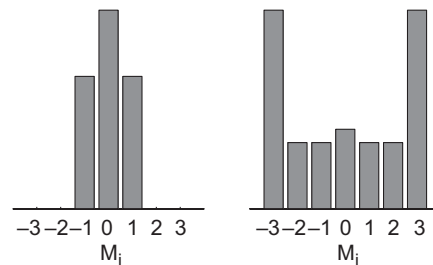


Figure 8.  $M_i$  populations of the  $3_2$  level in the  $\tilde{B}^1E''$  state that result in the parallel polarization geometry (left) and the perpendicular polarization geometry (right).

photoelectron distribution with a single radial feature [20], but not for more complicated photoelectron images of the kind obtained in this work. It is not possible to say at this stage whether the minor discrepancies observed are due to imperfections in the set of dynamical parameters, or imperfections in the data processing; work is ongoing with the latter. We emphasize that it is only because of the availability of a full set of dynamical parameters (Table 2) that the predictions shown in Figure 6(b) are possible. For most situations tomographic reconstruction of distributions resulting from a variety of polarization geometries will be essential to the determination of photoionization dynamics.

Comparison of parallel and perpendicular geometries allows an assessment of the alignment sensitivity of the PADs, which in turn tells us whether the emitted photoelectron is sensitive to the orientation of the molecular axis. Changing the polarization geometry from parallel to perpendicular rotates the distribution of  $M_i$  sublevels in the  $\tilde{B}^1E''$  state by  $90^\circ$  with respect to the polarization of the probe laser, where  $M_i$  is the component of the rotational angular momentum vector along the polarization vector of the probe laser, as well as generating coherences [28]. The  $M_i$  distributions in the two geometries are illustrated in Figure 8 where it can be seen that in the parallel geometry the  $M_i = 0$  level has the maximum population, whereas in the perpendicular geometry the  $M_i = \pm N_i$  levels have maximum population. The effect of this change on the PADs resulting from the  $1_1 \rightarrow 3_2$  transition is illustrated in Figure 9. Here, two-dimensional slices through the tomographically reconstructed PADs are compared with the parallel polarization result for four ion rotational states. It can be seen that the sensitivity to alignment depends on ion rotational state. The  $2_1$  and  $4_1$  ion states show very little alignment sensitivity. The  $5_4$  state shows no alignment sensitivity in the plane containing the probe polarization vector (the  $z$  axis), but does show alignment sensitivity in the  $xy$  plane.

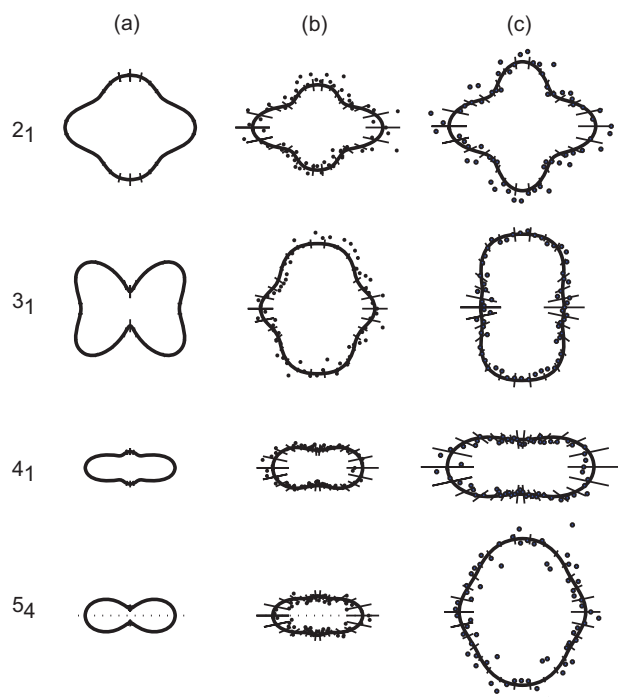


Figure 9. Comparison of two-dimensional photoelectron angular distributions for the parallel and perpendicular polarization geometries: (a) parallel polarizations, (b) perpendicular polarizations,  $xz$  plane, (c) perpendicular polarizations,  $xy$  plane. In the parallel case the PADs are taken from Figure 4. In the perpendicular case a slice through the tomographically reconstructed three-dimensional PAD was taken and data points corresponding to this are shown, with the solid line the fit to Equation (3). All distributions shown are for the  $1_1 \rightarrow 3_2 \text{ } \tilde{X}^1A_1'' \rightarrow \text{B } ^1E''$  ( $v_2=4$ ) transition, with labelled ion rotational states.

The most alignment sensitivity is observed for the  $3_1$  ion state. The appearance of the  $3_1$  state can be explained through atomic-like selection rules, and it is expected to be alignment-sensitive through its sensitivity to the orientation of the Ryberg state orbital angular momentum. It is however surprising therefore that the other ion rotational levels, whose appearance can also be attributed to the Rydberg character, show little alignment sensitivity, and this observation contrasts with the expectations of our earlier work [22]. Because the  $3_1$  and  $5_4$  peaks are relatively weak in the photoelectron spectrum (Figure 3) alignment sensitivity would be significantly reduced for the  $1_1 \rightarrow 3_2$  transition if rotational states were not resolved. This conclusion is of relevance to experiments in which PADs are proposed as probes of aligned molecules [29, 30].

## 6. Conclusion

The work presented here shows not only the utility, but the *requirement* for rotational resolution in studies of

photoionization dynamics in situations in which measurements from molecules whose orientation is fixed cannot be made. In this case we have been able to use the PADs correlated with the formation of individual ion rotational levels to obtain the dynamical parameter set which completely describes the ionization process. These parameters have been verified by comparison with rotationally resolved photoelectron spectra and angular distributions obtained using perpendicular polarization geometry. As well as providing tests of *ab initio* calculations, such parameters thus provide a means to calculate unmeasured quantities. We have also demonstrated the application of tomographic reconstruction to photoelectron images measured in non-cylindrically symmetric conditions as a means of overcoming the symmetry requirements of the standard image inversion routines. This technique is expected to be of general utility, and enables experimentalists to exploit multiple polarization geometries in the course of studying photofragmentation dynamics.

## Acknowledgements

We are extremely grateful to Dave Townsend and Jonathan Midgley for their assistance with this work. Funding was provided by the EPSRC under grant EP/C50013X.

## References

- [1] P. Hockett, M. Staniforth, K.L. Reid and D. Townsend, *Phys. Rev. Lett.* **102**, 253002 (2009).
- [2] S.L. Anderson, G.D. Kubiak and R.N. Zare, *Chem. Phys. Lett.* **105**, 22 (1984).
- [3] G. Ohrwall and P. Baltzer, *Phys. Rev. A* **58**, 1960 (1998).
- [4] D.J. Leahy, K.L. Reid and R.N. Zare, *J. Chem. Phys.* **95**, 1757 (1991).
- [5] H. Park and R.N. Zare, *J. Chem. Phys.* **104**, 4568 (1996).
- [6] A.T.J.B. Eppink and D.H. Parker, *Rev. Sci. Instrum.* **68**, 3477 (1997).
- [7] J. Zhou, E. Garand and D.M. Neumark, *J. Chem. Phys.* **127**, 7 (2007).
- [8] A. Osterwalder, M.J. Nee, J. Zhou and D.M. Neumark, *J. Chem. Phys.* **121**, 6317 (2004).
- [9] C.J. Hammond and K.L. Reid, *Phys. Chem. Chem. Phys.* **10**, 6762 (2008).
- [10] P. Hockett, M. Staniforth and K.L. Reid (in preparation).
- [11] M.N.R. Ashfold, R.N. Dixon, R.J. Stickland and C.M. Western, *Chem. Phys. Lett.* **138**, 201 (1987).
- [12] W. Habenicht, G. Reiser and K. Mueller Dethlefs, *J. Chem. Phys.* **95**, 4809 (1991).
- [13] H. Dickinson, D. Rolland and T.P. Softley, *J. Phys. Chem. A* **105**, 5590 (2001).

- [14] R. Seiler, U. Hollenstein, T.P. Softley and F. Merkt, *J. Chem. Phys.* **118**, 10024 (2003).
- [15] M.K. Bahng, X. Xing, S.J. Baek, X.M. Qian and C.Y. Ng, *J. Phys. Chem. A* **110**, 8488 (2006).
- [16] R. Signorell and F. Merkt, *Mol. Phys.* **92**, 793 (1997).
- [17] K.L. Reid, *Annu. Rev. Phys. Chem.* **54**, 397 (2003).
- [18] S.M. Bellm and K.L. Reid, *Chem. Phys. Lett.* **395**, 253 (2004).
- [19] G.A. Garcia, L. Nahon and I. Powis, *Rev. Sci. Instrum.* **75**, 4989 (2004).
- [20] M. Wollenhaupt, M. Krug, J. Kohler, T. Bayer, C. Sarpe-Tudoran and T. Baumert, *Appl. Phys. B* **95**, 647 (2009).
- [21] B.J. Whitaker, *Imaging in Molecular Dynamics: Technology and Applications* (Cambridge University Press, Cambridge, 2003).
- [22] D. Townsend and K.L. Reid, *J. Chem. Phys.* **112**, 9783 (2000).
- [23] S.W. Allendorf, D.J. Leahy, D.C. Jacobs and R.N. Zare, *J. Chem. Phys.* **91**, 2216 (1989).
- [24] P. Hockett and K.L. Reid, *J. Chem. Phys.* **127**, 154308 (2007).
- [25] S.N. Dixit and V. McKoy, *J. Chem. Phys.* **82**, 3546 (1985).
- [26] H. Park and R.N. Zare, *J. Chem. Phys.* **104**, 4554 (1996).
- [27] D.J. Leahy, K.L. Reid, H.K. Park and R.N. Zare, *J. Chem. Phys.* **97**, 4948 (1992).
- [28] K.L. Reid, D.J. Leahy and R.N. Zare, *J. Chem. Phys.* **95**, 1746 (1991).
- [29] J.G. Underwood and K.L. Reid, *J. Chem. Phys.* **113**, 1067 (2000).
- [30] T. Suzuki, *Annu. Rev. Phys. Chem.* **57**, 555 (2006).
- [31] R.N. Zare, *Angular Momentum* (Wiley, New York, 1988).

## Appendix 1

The experimentally deduced  $\beta_{LM}$  values, which are normalized to the angle-integrated intensities  $\beta_{00}$ , are fit to Equation (4) below in order to determine the values of  $r_{\lambda}$  and  $\eta_{\lambda}$  listed in Table 2. Equation (4) is also used to predict the PADs for the perpendicular geometry, using the parameters in Table 2

$$\begin{aligned}
 & B_{LM}(N_i, K_i, N^+, K^+) \\
 &= \sum_{l'l'} \sum_{\lambda\lambda'} \sum_{mm'} \sum_{N_i N_i'} \sum_{\mu\mu'} \sum_K (-i)^{l'-l} (-1)^{m+K+N_i'-M_i} \\
 & \times \frac{[2N_i+1](2N^++1)(2l'+1)(2L+1)(2K+1)]^{1/2}}{(4\pi)^{1/2}} \\
 & \times \begin{pmatrix} l & l' & L \\ m & -m' & M \end{pmatrix} \begin{pmatrix} l & l' & L \\ 0 & 0 & 0 \end{pmatrix} \begin{pmatrix} N_i & N_i' & K \\ -M_i & M_i' & M \end{pmatrix}
 \end{aligned}$$

$$\begin{aligned}
 & \times \begin{Bmatrix} N_i & N_i & N^+ \\ N_i & N_i' & K \end{Bmatrix} C(l, \lambda, m, N_i, \mu) C(l', \lambda', m', N_i', \mu') \\
 & \times T_{KM} r_{\lambda} r_{\lambda'} \exp[i(\eta_{\lambda} - \eta_{\lambda'})],
 \end{aligned} \tag{4}$$

where

$$\begin{aligned}
 \beta_{LM} &= \beta_{LM}(N_i, K_i, N^+, K^+) = \frac{B_{LM}(N_i, K_i, N^+, K^+)}{B_{00}(N_i, K_i, N^+, K^+)}, \\
 \beta_{00} &= B_{00}(N_i, K_i, N^+, K^+).
 \end{aligned}$$

In Equation (4),

$$\begin{aligned}
 C(l, \lambda, m, N_i, \mu) &= (-1)^{\mu} (2N_i + 1) \begin{pmatrix} l & 1 & N_i \\ m & -\mu_0 & M_i \end{pmatrix} \\
 & \times \begin{pmatrix} l & 1 & N_i \\ \lambda & -\mu & K_i \end{pmatrix} \begin{pmatrix} N^+ & N_i & N_i \\ K^+ & -K_i & -K_i \end{pmatrix}
 \end{aligned} \tag{5}$$

and

$$T_{KM} = D_{M0}^K(0, \Theta, 0) T_{M0}, \tag{6}$$

$$\begin{aligned}
 T_{K0} &= \sum_{M_i} (-1)^{N_i-M_i} (2K+1)^{1/2} \begin{pmatrix} N_i & N_i & K \\ M_i & -M_i & 0 \end{pmatrix} \\
 & \times \rho_{M_i M_i}(N_g, K_g, N_i, K_i).
 \end{aligned} \tag{7}$$

$D_{M_1 M_2}^J(\alpha, \beta, \gamma)$  is a Wigner rotation matrix element, with  $\alpha$ ,  $\beta$  and  $\gamma$  defining the Euler angles required for a frame rotation [31].  $N_i$  is the total angular momentum of the  $\tilde{B}^1E''$  state, excluding spin, with  $M_i$  its projection in the lab frame, and  $N_i$  and  $M_i$  are angular momentum transfer terms. The  $T_{KM}$  parameters define the alignment of the prepared state; this alignment depends, through the density matrix elements  $\rho_{M_i M_i}$ , on the number of photons used in the excitation step (two in this case), the polarization of the light, and the angle,  $\Theta$ , between the lab frame  $Z$  axes in the frames of the pump and probe beam. In the case of linear polarization the  $Z$  axis is defined to be along the relevant polarization vector. If the two frames are coincident, and there is no alignment prior to excitation (the latter is assumed in Equation (6)), then  $M=0$  and the diagonal density matrix elements,  $\rho_{M_i M_i}$ , can be defined by

$$\rho_{M_i M_i}(N_g, K_g, N_i, K_i) = S(N_g, K_g, N_i, K_i) \begin{pmatrix} N_g & 2 & N_i \\ -M_g & \mu_0 & M_i \end{pmatrix}^2, \tag{8}$$

where  $S(N_g, K_g, N_i, K_i)$  are the rotational linestrength factors [11] and  $\mu_0$  denotes the photon polarization (0 in this case, so that  $M_i = M_g$ ). For perpendicular polarization vectors coherences are generated and  $M$  can take the values 0, 2 and 4.